



Manipulating the geometry of architected beams for maximum toughness and strength

Ahmed S. Dalaq^a, Francois Barthelat^{a,b,*}

^a Department of Mechanical Engineering, McGill University, 817 Sherbrooke Street West, Montreal, QC H3A 2K6, Canada

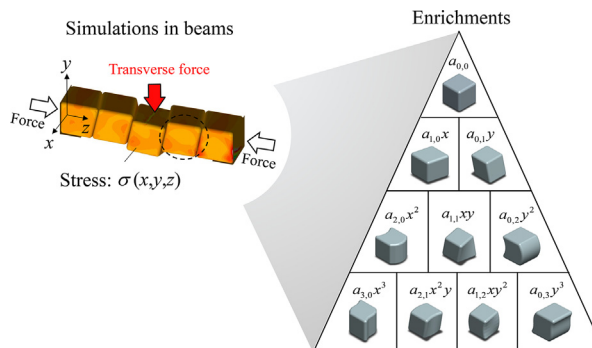
^b Department of Mechanical Engineering, University of Colorado, 427 UCB, 1111 Engineering Dr, Boulder, CO 80309, United States



HIGHLIGHTS

- Interlocking of blocks can be achieved by enriching architected beams with blocks having curved and wavy contact surfaces.
- The contact surfaces of blocks can be characterized by a waviness parameter ϕL which correlates with toughness and strength.
- Weak blocks allow little interlocking therefore toughness is achieved through deformation.
- Strong blocks allow interlocking therefore both strength and toughness are achieved through hardening.
- Architected beams fail progressively resulting in 370 times the toughness and 40% the strength of the monolithic beam.

GRAPHICAL ABSTRACT



ARTICLE INFO

Article history:

Received 17 December 2019

Received in revised form 11 June 2020

Accepted 14 June 2020

Available online 20 June 2020

Keywords:

Architected materials

Segmented materials

Structural stability

Topologically interlocking materials (TIMs)

ABSTRACT

Dense architected materials are made of blocks that can slide, rotate, interlock and jam in powerful mechanisms that can generate simultaneous strength and toughness. Nature abounds of examples of such architected materials, for example in the segmented structure of vertebrate spines. In this study we consider segmented beams made of stiff blocks and submitted to a transverse force. We start with simple cubes as a geometrical reference, which we then enrich by using two-dimensional polynomial functions. The flexural response of the beam is simulated using finite element modeling (FE-model) to predict strength, toughness and maximum local stresses. Using this procedure we identified the most efficient interface geometries and interlocking mechanisms within a set of polynomial functions and for a given strength of the individual blocks. To illustrate these results, we fabricated segmented beams of ceramic glass using a laser engraver. Experiments on these architected glass revealed how enriched blocks turned the catastrophic brittle failure of monolithic glass into graceful progressive deformation. Resulting in a tougher response than the monolithic by 370 times and preserved 40% of strength of that of the monolithic.

*Corresponding author.

© 2020 Published by Elsevier Ltd. This is an open access article under the CC BY-NC-ND license (<http://creativecommons.org/licenses/by-nc-nd/4.0/>).

* Corresponding author at: Department of Mechanical Engineering, McGill University, 817 Sherbrooke Street West, Montreal, QC H3A 2K6, Canada.

E-mail address: francois.barthelat@colorado.edu (F. Barthelat).

1. Introduction

Toughness and strength are mutually exclusive properties in engineering materials. For example ceramics are hard and strong against deformation, but they can only undergo small deformation and they are brittle. For many applications there is a pressing need to combine strength and toughness in one material, especially when materials are subjected to unanticipated loads. Weight is an equally important property to minimize in order to reduce carbon emissions of vehicles, produce more slender structures and allow for bolder outer space explorations. For reducing weight, many brittle materials such as glass, clay and some ceramics are relatively light and inexpensive [1]. While these materials are brittle they are also relatively stiff, corrosion resistant, abrasion resistant and have low thermal expansion [2,3]. Some of these materials, for example glasses, are also transparent. The toughening of these brittle materials is a major challenge which may allow their use as structural components: beams, shock absorbers, trusses and frames. Architected and segmented materials are powerful approaches to toughen brittle materials (Fig. 1a). Segmentation is prominent in masonry structures, particularly in monuments, shear walls and domes [4,5]. In addition, the field of pavement design is rich with design templates and tessellations applicable to architected materials [6]. Masonry structures have recently inspired topologically interlocked materials (TIMs) which rely on the geometrical interlocking

of relatively stiff blocks [7–9]. TIMs can contain cracks and improve toughness [7–13]. The shapes of individual blocks range from simple cubes, tetrahedrons, octahedron to more complex osteomorphic blocks [11,14,15] (Fig. 1b). Individual blocks are relatively stiff, and their deformations are typically small and within elastic limits. However the interfaces between the blocks are more compliant and weaker, so they can channel deformations and arrest cracks [16–19]. The blocks can also rotate (hinge), slide, separate, interlock and jam, generating powerful mechanisms for improving toughness and strength [11,20–22]. The blocks may be held together and confined by external ligaments such as stiff frames, internal tension cables, pre-compressed supports to manipulate contact and friction forces [9,23–26]. One drawback of tension cables is that it may interfere with the sliding and rotation action of blocks. A practical alternative is to use variable spring support [27], a device used in pipelines that can effectively serve as a support and exert a controlled precompression on architected beams (Appendix A.5, Fig. A.5). Architected materials and structures are information-rich and highly tunable (e.g. dimensions, shapes, elastic modulus, surface friction and number of blocks), a feature which suits itself to optimization.

Interestingly, hard natural materials such as wood, mollusk shells, bone, teeth or even entire skeletons are also made of stiff but brittle “building blocks” with remarkably uniform geometries and arrangements [17,28,29]. The interaction of shape, size, composition,

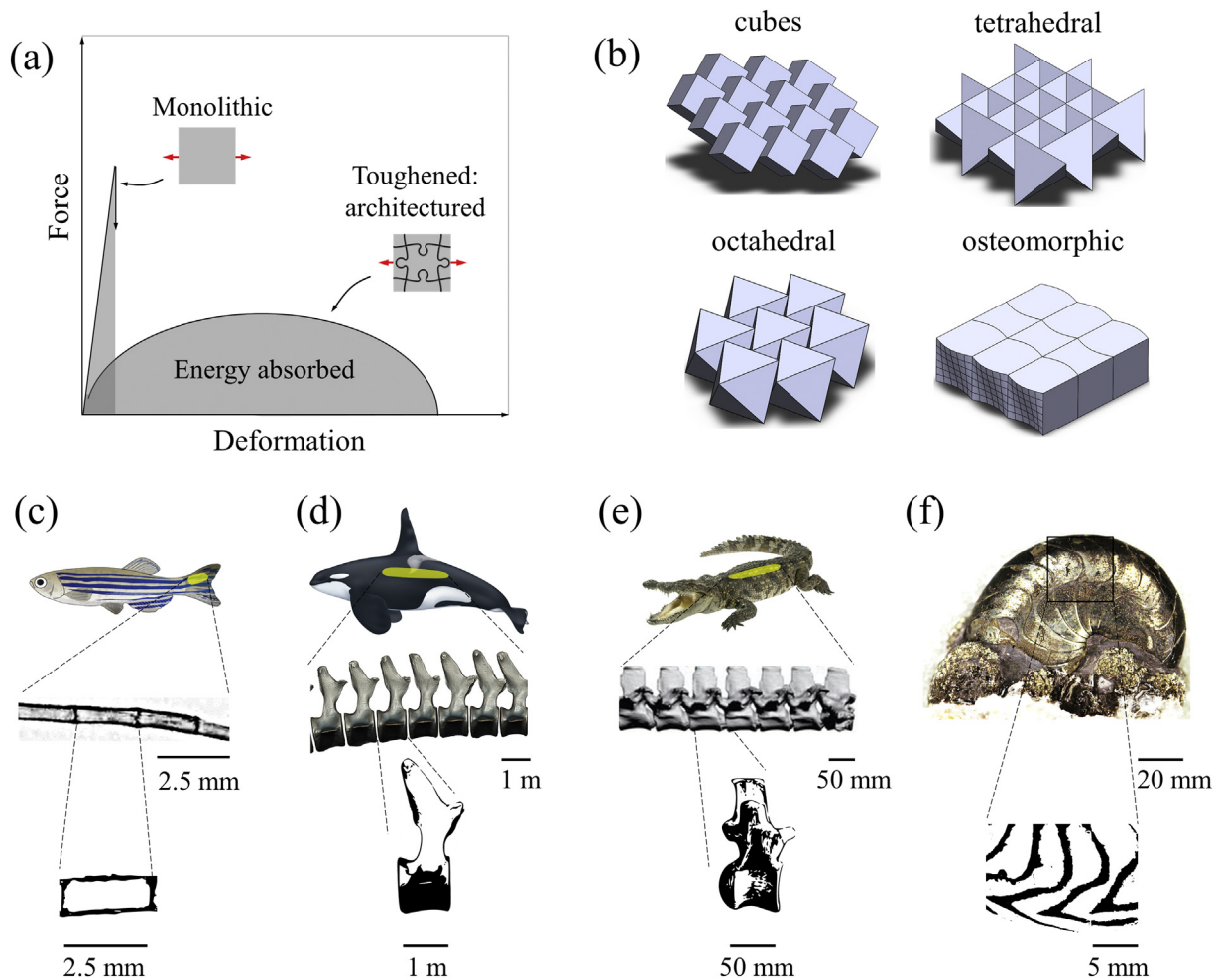


Fig. 1. (a) Typical force–displacement curves of architected materials versus monolithic materials; (b) topologically interlocked materials (TIMs). Linearly segmented architected materials in nature: (c) fish fins of zebrafish (adapted from [45]), (d) vertebrae of orca (adapted from [35]), (e) concavo-convex vertebrae in the spines of crocodiles (adapted from [40]) and (f) goniattite (adapted from [37]).

orientation, arrangement of blocks, interface geometry along with soft protein bonding at the interfaces which can generate nonlinear visco-elastic and contact-based deformations, lead to remarkable combinations of stiffness, strength and toughness. The arrangement of the blocks vary from linear arrays as in fish fins and spines [30–33] (Fig. 1c) to 2D arrangement like the tesserae in sharks [34] to more complex decussations of mineralized rods in teeth enamel [17]. Both fish fins and vertebrate spines are composed of mineralized blocks arranged linearly and bonded with soft collagenous membranes (Fig. 1c, d, e) [30–33]. The shape of the blocks, and specifically the geometry of the interface, may vary across species and biological components, giving rise to specific properties and functionalities (Fig. 1c, d, e, f). The geometry of the interface may vary from straight interfaces as in fish fins and vertebrae of orcas (Fig. 1c, d), to slightly curved interfaces in crocodiles (Fig. 1e) to complex serrated sutures between blocks in ammonites (Fig. 1f) [36,37]. Some reptiles including crocodiles have concave and/or convex round interfaces between their vertebrae [38–40], which allows for a high range of motion for their spine. Applications of such segmented materials and structures include armor, domes, glass facades, shields, robotic arms, deployable and anti-seismic columns [17,26,41]. In addition to segmentation, these systems are sometimes loaded with pre-compression. For example armored panels are subjected to pre-compression in the in-plane direction for improved damage tolerance [42]. Spines, domes and structural columns are compressed under their own weight and from the weight of the elements they carry [4,5]. In addition, in a previous study we found that the effect of precompression is limited to increasing stability and effective strength [43]. On the other hand, the slightest variation in the geometry of the blocks can induce profound changes to the overall response [43].

Previous studies applied strategies of nature in architected materials achieved some improvements, but at the expense of strength [9,12,44]. In particular, linearly segmented materials similar to spines have not been studied extensively to this day. In a previous study, we found that the behavior of a segmented beam depends on the number of blocks, friction and interface designs between blocks [43]. We also found how the segmentation of glass panel into rectangular prisms with flat interfaces improves toughness, strength and the damage tolerance of glass [41]. In a previous study we found that failure of architected beams is strongly dependent on the number of blocks and friction between blocks [43]. Another important aspect of segmented materials is the geometry and arrangement of the blocks (architecture). Our previous study showed that curved interfaces have an effect on failure mode, particularly it prevents the undesired hinging failure mode [43], and that they also induce block jamming during deformation [43]. Hinging involves rotation of blocks around few localized points, making the contribution of the geometry of interfaces minimal. It also localizes stresses making it unfit for brittle materials [43]. Whereas, in sliding failure mode, entire interface interacts by sliding, jamming and interlocking, and therefore is highly affected by geometry. Therefore, we focus here on the effects of geometry on systems that undergo sliding failure mode. These previous studies were also limited to two-dimensional geometries and to interfaces with a single curvature. In addition, they ignored internal stresses in individual blocks and their potential failure. Several aspects such as failure of blocks, the level of interlocking between blocks, the overall mechanical behavior (force-displacement curves), strength, toughness, stability and their possible dependence on strength of blocks remained unexplored. The effects of three-dimensional geometrical enrichments of the contact surfaces on overall mechanical response are not well understood. In this study we systematically enrich the 3D geometry of the interfaces between the blocks to explore and optimize interlocking mechanisms between the blocks and mechanical performance (strength, toughness and stability).

To carry out a systematic study on the effect of geometry of blocks we consider here an ideal array of 5 blocks with tunable contact

interfaces described by 2D-polynomials. We fixed the study to 5 blocks to ensure a sliding failure mode and to avoid hinging. This structure may not serve as an all-ready structure for service, per se, but rather it represents and simulates the behavior of linearly segmented “materials”, which is a form of architected materials that may comprise beams, columns and similar prismatic structural components.

2. Model setup and enrichment of cubes with fillets

For this study we considered idealized segmented beams composed of $N = 5$ identical blocks with dimensions $L \times L \times L$. The blocks are aligned in a single row between two rigid supports (Fig. 2a). They are modeled as linear elastic (modulus E , Poisson's ratio ν), with contact elements inserted at the interfaces between the blocks, and also between the end blocks and the rigid supports. The end supports are used to impose a pre-compression force F_A that holds the row of blocks in place by dry friction (friction coefficient f). To assess the strength and stability of this segmented beam we apply a transverse displacement u at the center of the beam (coordinates $(5L/2, L/2, L/2)$) that is progressively increased until collapse of the system. The corresponding reaction force is the transverse force F_T which is recorded at each increment of the transverse displacement u .

A simple starting point for this study is a segmented beam made of cubes, a system we recently investigated to reveal the importance of friction and number of blocks on overall strength, failure mode and stability [43]. 3D finite element models (FE-model) with different fillet radii were automatically generated and simulated using a combination of Matlab and Ansys-APDL (Appendix A.1). Mesh convergence was verified in all the results presented in this report. Since the state of stress in the system have no particular length scale, all dimensions were normalized by the size of the blocks L . It is known from the contact mechanics of elastic punches [23,24] that the contact stresses at the corners of cubes are infinite. To prevent the stress from reaching these singularities and for a more realistic model, we rounded all edges and corners of the cubes with a fillet of radius r/L (Fig. 2b). These fillets enabled stress convergence at the edges and corners of the cubes, and also ensured mesh independent results. Rounding of the corners and edges of the blocks acted as a first level of geometrical enrichment for the cube-based segmented beams, with significant impact on the strength and stability of the architected beam. To assess the effect of fillet radius r/L we ran FE-models for beams made of blocks with $r/L = 0.05, 0.1, 0.2, 0.3, 0.5$. The sliding of the blocks is governed by frictional forces, which are in turn governed by the pre-compression F_A . More specifically, we verified that the transverse force is proportional to the axial pre-compression, so that the results can be displayed as normalized force F_T/F_A without loss of generality. The force-displacement curves, $F_T - u$ for different r/L show a linear increase in transverse force F_T (for $r/L < 0.5$) until a maximum F_T is reached at the onset of sliding (Fig. 2c). After this linear elastic part, the block(s) start sliding progressively (Fig. 2d), which is associated with a decrease of the compressive force F_A : sliding the blocks reduces the volume of elastically deformed material held between rigid supports which in turn decreases the axial stiffness of the beam. As a result of the decrease of axial force the friction force at the interface decreases, and F_T decreases almost linearly with increasing u (Fig. 2c). At a critical displacement the sliding block (s) completely loses contact and the center block is being pushed out (first column on Fig. 2d for $u/L = 0.85$). At this point the transverse force becomes compressive ($F_T < 0$) which indicates the tendency of the sliding blocks(s) to “eject” out of the system. This general $F_T - u$ behavior was observed for all radii $0.1 < r/L \leq 0.5$, but the specific overall properties of the beam varied with r/L . Increasing r/L led to a significant decrease in initial stiffness, to a slight decrease in strength, and to a more rapid instability in the system. For example, increasing the fillet radius from $r/L = 0.1$ to $r/L = 0.3$ decreased the maximum displacement by 50% (Fig. 2c). For $r/L = 0.3$, a group of blocks sled and gradually started rotating, which are signs that the system is transitioning from a

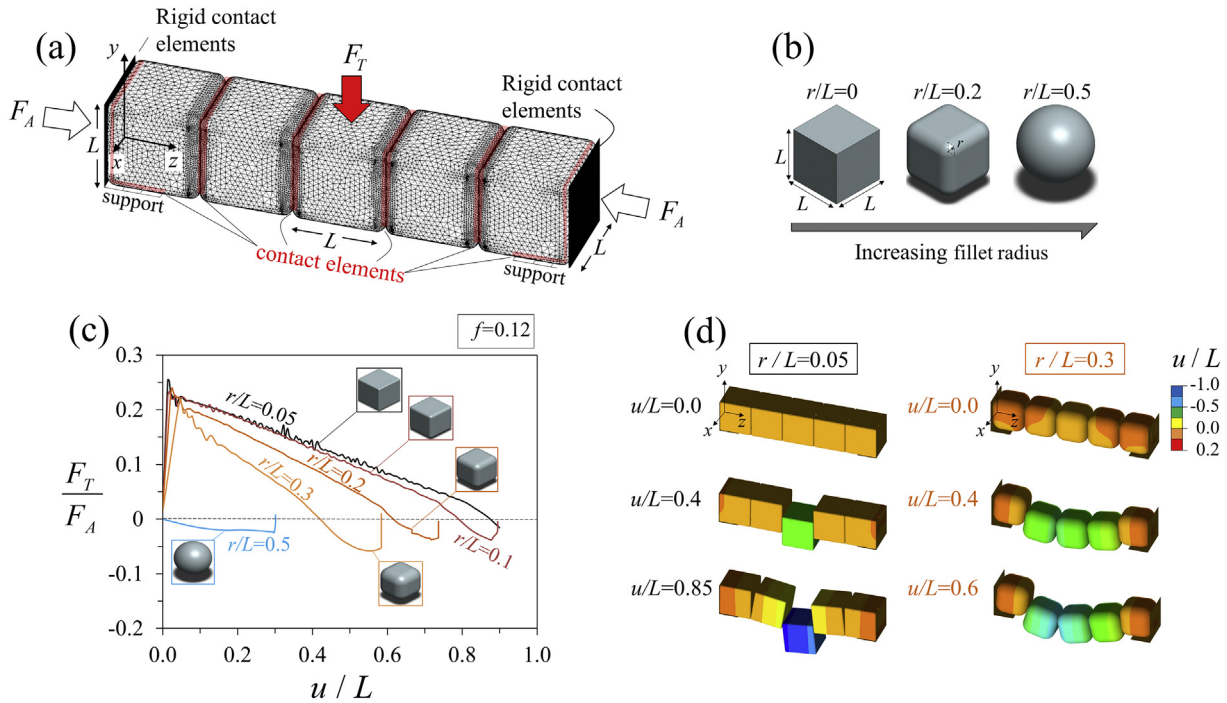


Fig. 2. (a) Finite element model: blocks are meshed and mesh refinement is applied at edges and corners; (b) the cube is enriched by rounding the edges and corners with fillets from $r/L = 0$ to $r/L = 0.5$ where finally the cube is transformed into a sphere. Effect of applying fillets r/L on (a) $F_T - u$ curves and (b) deformation.

sliding failure mode into a “hinging” failure mode [43] (second column on Fig. 2d). Sphere-based beams ($r/L = 0.5$) are highly unstable and the transverse force is negative over the entire simulation. In these simulations we also monitored the maximum tensile stresses $(\sigma_1)_{\max}$ occurring within the blocks, in order to predict damage and fracture (we assumed brittle blocks). A typical snapshot from FE – model of the maximum (principal) stress contours for $r/L = 0.3$ and at $u/L = 0.5$ is shown on Fig. 3a. As expected from the contact mechanics of frictional sliding, the maximum tensile stress occurs at the trailing edge of the contact area. Fig. 3b shows the evolution of the maximum tensile principal stress during deformation for different r/L . We verified that the maximum stress $(\sigma_1)_{\max}$ is proportional to F_A , so we used $(\sigma_1 L^2 / F_A)_{\max}$ as a non-dimensional number to characterize the maximum principal stresses in the blocks. These stresses increase linearly with u/L until the onset of sliding at $u/L = 0.035$ marking the first peak, after which

$(\sigma_1)_{\max}$ falls sharply. The stresses then increased gradually as the contact area decreased and the contact pressure increased. The maximum stress reached another maximum value well into the sliding of the blocks at $u/L > 0.4$ (marked with a red dot on Fig. 3b). Afterward the stress decreased continuously until complete failure. In general the maximum stress was the highest for small r/L , except for the extreme case $r/L = 0.5$ (sphere) where the maximum stresses were comparatively very high.

Assuming that the blocks are made of a brittle material, we used a simple failure criterion: the blocks fractured when the maximum principal stress exceeds the tensile strength σ_s/E . We therefore truncated the $F_T - u$ curves at the point at which $(\sigma_1)_{\max}/E \geq \sigma_s/E$, and the remaining first part of these curves were used to compute the toughness U_{\max} and the strength F_{\max} (Appendix A.2, Fig. A.2). Fig. 4 shows a toughness-strength map for segmented beams made of blocks with

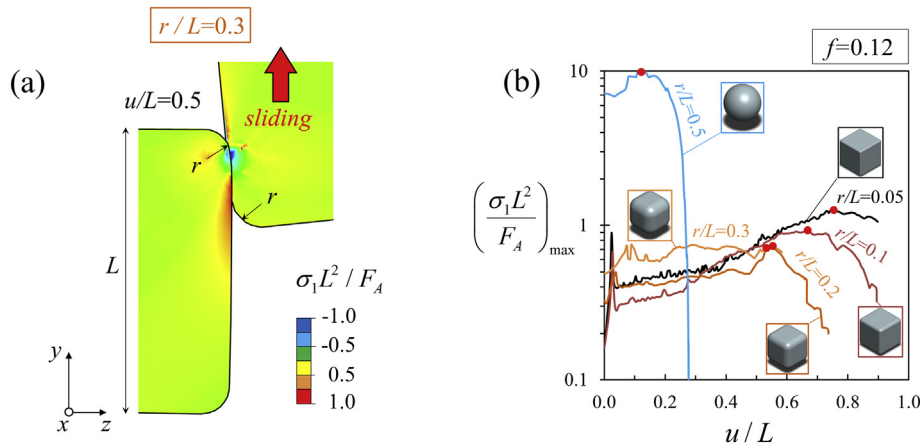


Fig. 3. Normalized maximum principal stresses in the segmented beam during deformation; (a) stress contours in the blocks at $u/L = 0.5$ for $r/L = 0.3$; (b) maximum principal stress variation during deformation, $(\sigma_1)_{\max} - u$ curves, the point of maximum stress is denoted by a red dot marker.

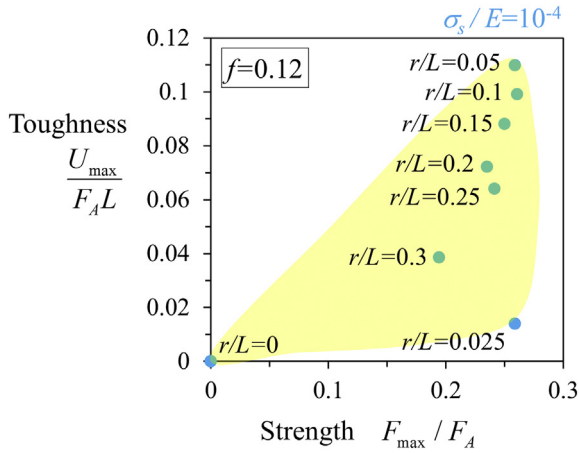


Fig. 4. Toughness–strength map for segmented beams made of blocks with different rounding r/L .

different rounding. The case with no rounding ($r/L = 0$) and perfectly sharp cubes is a theoretical case where the stresses are infinite, and where the blocks immediately fracture upon sliding. As a result the toughness and strength are zero for $r/L = 0$ (Fig. 4b). For $r/L = 0.025$, the stresses are high, the blocks therefore fracture which results in a truncated $F_T - u$ curve with little deformation. Conversely, for $r/L = 0.05$, the stresses are lower than $r/L = 0.025$ where the beam deformed without fracture, resulting in the highest toughness and highest strength. For $0.1 \leq r/L < 0.3$, the inherent lower maximum force and displacement of these cases result in lower strength and toughness than $r/L = 0.05$. According to Fig. 4 the optimum values are $r/L = 0.025$ and $r/L = 0.05$ for highest strength and toughness respectively.

3. Geometrical enrichments with polynomial functions

Using the same approach for model generation, finite element modeling and data processing we then considered more complex geometric enrichments for the blocks. One objective was to generate progressive interlocking between the blocks, in order to achieve better combinations of strength and toughness. To enrich the geometry of the blocks we considered contact surfaces that followed polynomial equations of the form:

$$z(x, y) = \sum_{i,j} a_{i,j} x^i y^j \quad (1)$$

The contacting surfaces of every block followed Eq. (1), which ensured that the initial contact surfaces were conformal. Individual terms and their combinations can be visualized with the Pascal's triangle shown on Fig. 5. The curvature and waviness of the blocks are clearly more pronounced as the order of the monomial $i + j$ is increased. Enrichments that are a single function of x or y transform contact faces along a single direction resulting in a curved “extruded-like” designs, while multivariable monomials transform the contact faces in both directions resulting in more wavy designs. Both the deformation and $F_T - u$ curves generated by the finite element model was validated with experiments before conducting a full study on all designs (Appendix A.1, Fig. A.1).

Additional shapes can be generated by combining the monomials of Fig. 5. Because of the high computational cost of the densely meshed 3D-models we limited this study to binomials. We did not pursue single variable monomials along x as $z(x) = a_{i,0} x^i$ because they do not provide interlocking. Likewise, we excluded the hyperbolic-paraboloid: $z(y) = a_{1,1} xy$ which are unstable for large $a_{1,1}$. Asymmetric designs about y - z plane like $z(y) = a_{1,2} xy^2$ undergo extremely high stresses and allow for little sliding (limited deformation). In addition, the contact faces of

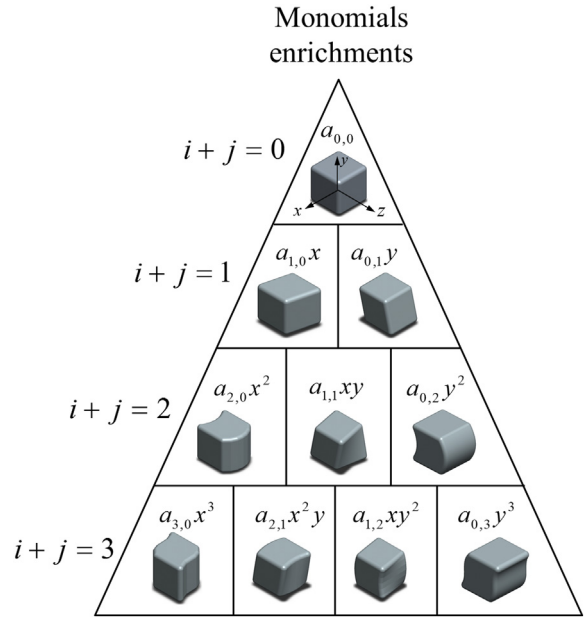


Fig. 5. Enriching the contact surfaces between blocks with 2D-monomial functions. Pascal triangle depicting individual terms; the degree of the polynomial $i + j$ increases from top to bottom.

the asymmetric designs channel forces along x -direction where there is no contact-based resistance at end supports to hold the structure together and maintain stability. We therefore excluded these asymmetric designs and considered only symmetric ones which are a total of 4 designs. We explored all possible combinations of these symmetric monomials. The order in combining these monomials is irrelevant therefore all possible combinations are given by; $C(2,4)$ combinations which results in a total of: $C(2,4) = 4! / 2! (4 - 2)! = 6$ combinations, where C represents combinations and $!$ represents the factorial. Fig. 6 shows the monomials we combined to form different binomials. The resulting binomial functions are shown above each design. The coefficients $a_{i,j}$ of the polynomial function can be varied to change the amplitude of the surface A , which can be found with:

$$A = |z(x_{max}, y_{max}) - z(x_{min}, y_{min})| \quad (2)$$

where x_{min} , y_{min} , x_{max} , and y_{max} are the x, y location of the maximum and minimum points of $z(x, y)$. The coefficient $a_{i,j}$ are varied such that the amplitude is $A/L \leq 0.5$. The edges and corners of all designs were rounded with a fillet radius of $r/L = 0.1$.

Fig. 7 shows some examples of $F_T - u$ curves for the enriched designs. Fig. 7a is a design with $z(x) = a_{2,0} x^2$, a profile that produces little interlocking along the sliding direction and which produces a response comparable to the cube cases described above. Designs that included terms that are a function of y were more successful: they generated a progressive interlocking that increased F_T during deformation (Fig. 7b). The axial compressive force decreases as the blocks slide, which decreases the efficacy of jamming between blocks. There is a competition between geometric hardening and softening during the loss of contact which results in a maximum force, followed by softening until complete failure. The progressive interlocking is more pronounced for the multivariable monomial: $z(x,y) = a_{1,2} xy^2$ (Fig. 7c), which is a wavy contact face. In addition, this multivariable monomial shows a more stable response, resulting in a maximum displacement that is 1.5 times higher than $z(y) = a_{0,2} y^2$ for $a_{i,j} = 0.4$. Adding a plane term: $z(y) = a_{0,1} y$ to the $z(y) = a_{0,2} y^2$ forms a tilted-parabolic profile for the contact faces that improved stability by prolonging the progressive interlocking during deformation (Fig. 7d). Finally, adding the cubic profile: $z(y) = a_{0,3} y^3$ to $z(x,y) = a_{1,2} xy^2$ generated more interlocking which increased the maximum force (strength) (Fig. 7e). For all cases,

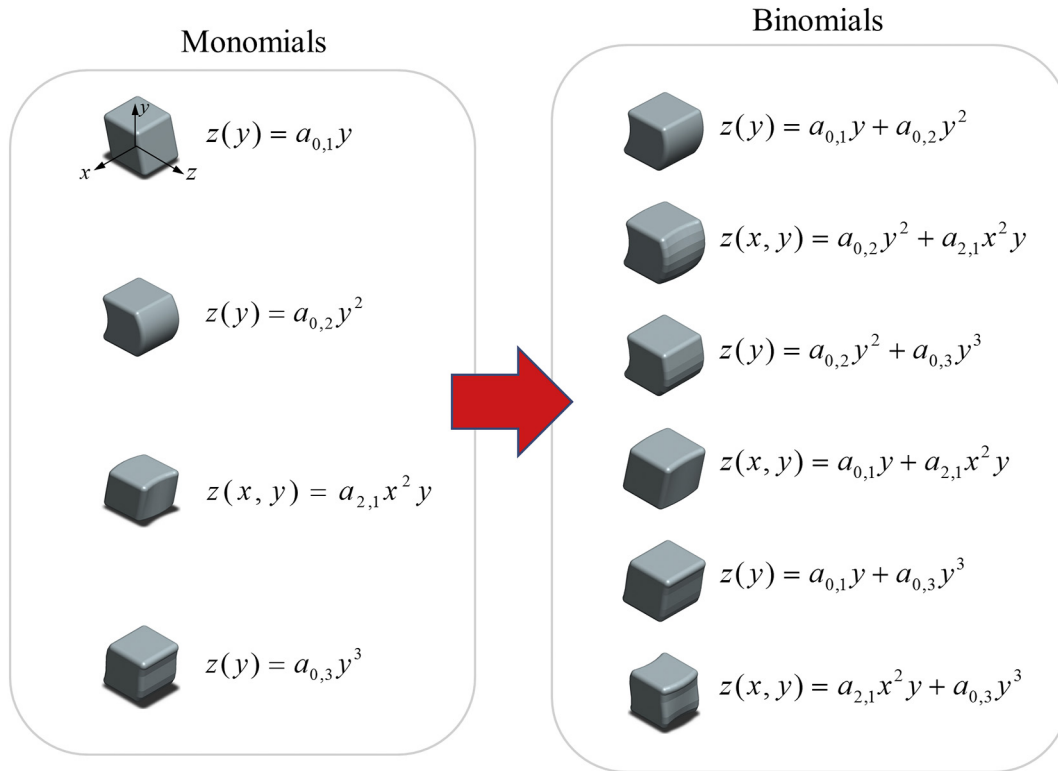


Fig. 6. Combining monomials to form binomials.

increased amplitude (higher a_{ij}) increased strength, but at the expense of maximum displacement (i.e. stability).

Fig. 7 highlights the profound effect of surface geometry on the mechanical response of the architected beams. It is then possible to rank the efficacy of these particular designs by strength, by toughness (total area under the $F_T - u$ curve), or by a combination of the two. Importantly we note that both F_{\max} and U_{\max} are directly proportional to the friction coefficient f , provided that $0 < f \leq 0.3$ and that the structures fail by sliding. Therefore, we normalized both F_{\max} and U_{\max} by f . Fig. 8a shows the maximum normalized strength and toughness for each design considered here. The cube-based designs produced the lowest strength and energy absorption, while the wavy design $z(x, y) = a_{2,1}x^2y + a_{0,3}y^3$ produced the highest strength and toughness. We previously studied round interfaces (concavo-convex geometry [43]) which generated improvement in strength and toughness. This simple round design (denoted by filled circular marker) underperformed compared to almost all multivariable wavy designs. For example it only achieved 0.07 the strength and toughness produced by blocks with waviness $z(x, y) = a_{2,1}x^2y + a_{0,3}y^3$. Fig. 8a shows that there is a strong correlation between strength and toughness for the designs tested here. The results suggest that wavier designs produced higher strength and toughness in comparison to flat and less curved designs. This observation may be confirmed quantitatively by considering a single geometric parameter to characterize the degree of “waviness” in the design. Here we define a normalized surface curvature ϕL , computed from derivatives of the surface in both directions, and which echoes the definition of curvature for 1D functions [46]:

$$\phi L = \frac{1}{L} \left\langle \frac{\partial^2 z}{\partial y^2} + \frac{\partial^2 z}{\partial y \partial x} \right\rangle \left(\frac{\partial z}{\partial y} + \frac{\partial z}{\partial x} \right) \quad (3)$$

The chevrons $\langle \rangle$ denote mean values computed over the entire surface. The numerator of Eq. (3) puts a stronger emphasis on variations along y to capture waviness along the loading direction. We calculated ϕL for different designs and Fig. 8b shows how wavier and curvier contact faces translate into higher ϕL values, and therefore we used ϕL as a metric for geometrical waviness of the different designs. It is then useful and instructive to assess how the single waviness parameter ϕL governs the mechanical performance of the architected beam.

Fig. 8c and d show the strength and toughness plotted as function of ϕL for the different designs explored here. The plots show that the waviness parameter ϕL can be used as an approximate predictor of strength and toughness for the architected beam. This feature can be useful to predict the efficacy of other designs without recourse to FE analysis. The scatter in the plots was attributed to the inherent instability of certain shapes. The friction coefficient f and the number of blocks N are the main contributors to changing the failure mode of such structures [43], therefore for sliding cases the waviness parameter ϕL may be general and applicable for predicting both toughness and strength of such architected beams. Further studies are needed to assess the applicability of ϕL for different enrichment types and/or different loading conditions.

4. Optimization of monomials and binomials for finite strength of blocks

A limiting factor in the amount of interlocking between the blocks is the strength of the blocks themselves. In order to bring this factor into the design of the blocks we tracked the stresses during the entire simulations. Fig. 9 shows the maximum principal stress $(\sigma_1)_{\max}$ during deformation for three designs. For the case $z(x) = a_{1,0}x$, the absence of interlocking along the loading direction leads to negligible stresses (Fig. 9a). For the curved design $z(x) = a_{2,0}x^2$, the maximum stress increases with interlocking, and once the interlocking diminishes, the maximum stress in the blocks diminishes as well (Fig. 9b).

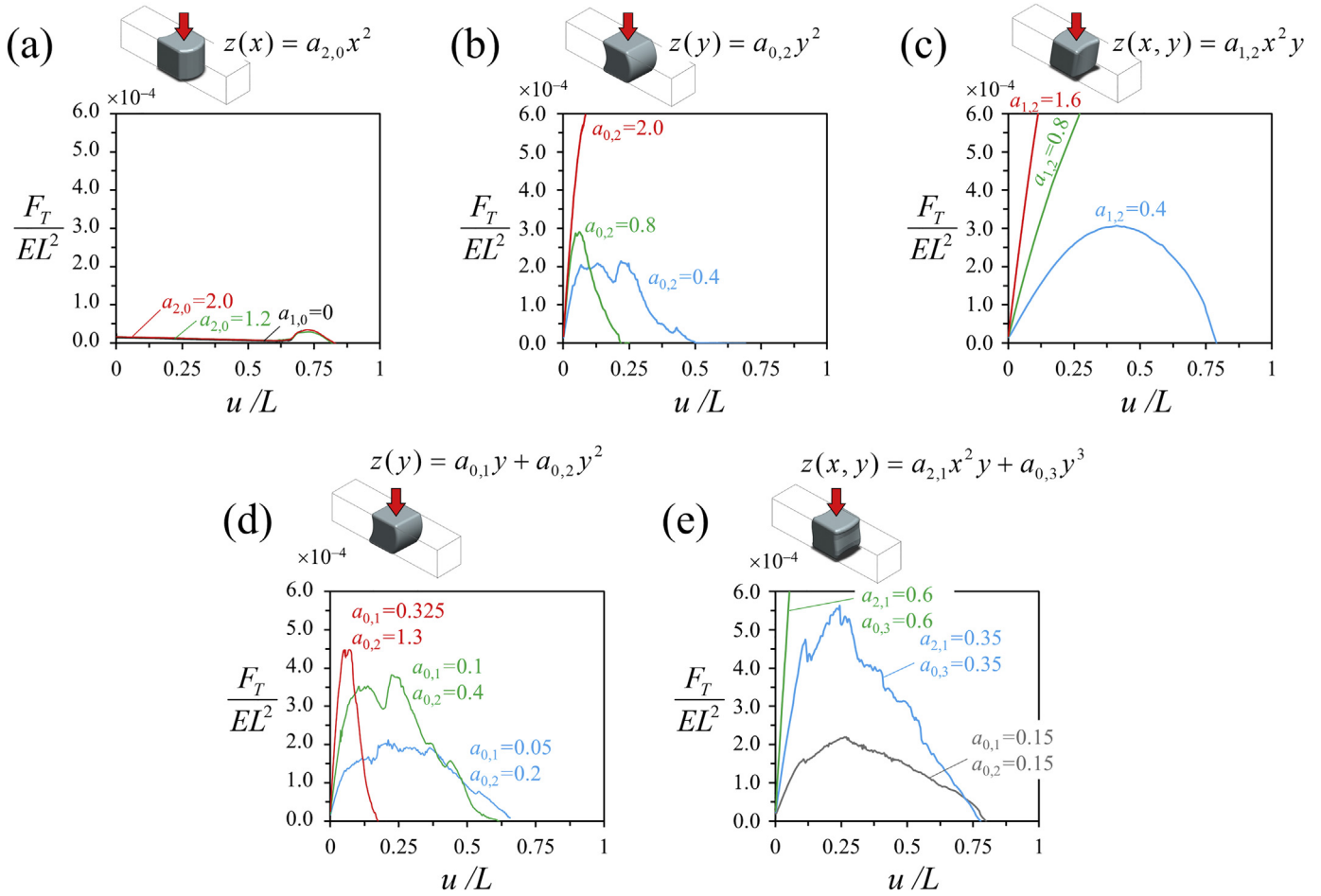


Fig. 7. Force–displacement, $F_T - u$ curves for (a) $z(x) = a_{2,0}x^2$, (b) $z(y) = a_{0,2}y^2$ and (c) $z(x,y) = a_{1,2}x^2y$, (d) $z(y) = a_{0,1}y + a_{0,2}y^2$ and (e) $z(x,y) = a_{2,1}x^2y + a_{0,3}y^3$; the plots are reported for $f = 0.12$.

For $z(x,y) = a_{1,2}xy^2$, sharper features at the contact faces (high ϕL) lead to more interlocking between blocks but also to high contact stresses.

The performance of each design depends not only on interlocking, but also on the strength of the blocks σ_s/E . Like section 2, we truncated the $F_T - u$ curves at the point at which $(\sigma_1)_{\max}/E \geq \sigma_s/E$, and the remaining first part of these curves were used to compute the toughness U_{\max} and the strength F_{\max} (Appendix A.2, Fig. A.2). For each design we explored about 25 combinations of different constants (i.e. different amplitudes, Appendix A.3, Fig. A.3b). The maximum strength and toughness were computed for three different strength levels σ_s/E , resulting in a total of 75 simulations for each design. For both monomials and binomials, the optimum design was found by plotting the data on $F_{\max} - U_{\max}$ space (Appendix A.3, Fig. A.3). Fig. 10 shows the performance for two examples, the cubic: $z(y) = a_{0,3}y^3$ and the monkey-saddle: $z(x,y) = a_{2,1}x^2y + a_{0,3}y^3$. For each geometry we considered three levels of strength: $\sigma_s/E = 10^{-4}, 10^{-3}, 10^{-2}$. The plots include the cube design $a_{i,j} = 0$ (flat contact faces) for comparison. The higher the σ_s/E , the higher the strength and toughness, because the blocks can withstand more stresses, and therefore they can undergo more interlocking and sliding during deformation. For each value of σ_s/E , there is an optimum design; a particular $a_{i,j}$ value on $F_{\max} - U_{\max}$ space that outperforms other designs. For each value of σ_s/E , the shape of the optimum design is shown adjacent to each optimum point along with the optimum $a_{i,j}$ value(s).

For each geometrical design and strength, we could therefore identify the optimum amplitudes $a_{i,j}$. The results are displayed on an Ashby plot for $\sigma_s/E = 10^{-4}, 10^{-3}, 10^{-2}$, designated by blue, red and

grey respectively (Fig. 11). For comparison, simulation results for a monolithic beam with the same dimensions, under same mechanical loads, including the same axial precompression ($F_A/EL^2 = 6 \times 10^{-5}$) and made of the same material are also shown (denoted by a “+” marker on each plot). Curved geometries along loading direction (z -direction) (e.g. Fig. 7b, c, d, e) can maintain stability and hardening even at absence of precompression, because blocks can jam and/or interlocking during deformation. Increased precompression F_A increases strength and toughness of all designs, due to increased efficacy of jamming and interlocking between blocks. However, the distribution, the ranking of these designs on the strength-toughness space (Fig. 11) may remain unchanged by variations of F_A . We first note that none of the architected designs exceed the strength of the monolithic beam, but also that many of them exceed the monolithic case in terms of toughness. The designs with best combinations of strength and toughness are highlighted in yellow on Fig. 11 within each of their strength groups. The distribution of these best designs indicates that there is a compromising relationship between strength and toughness that is more prominent for weak blocks $\sigma_s/E = 10^{-4}$ (Fig. 11a). For $\sigma_s/E = 10^{-4}$ (weak blocks), the cubes (denoted by empty square marker) absorbed 280 times more energy than the monolithic but lost 60% of strength. For best toughness, the monomials that are function of only x ($z(x)$) absorbed the highest energy. The absence of progressive interlocking in these monomials subjected their contact faces to lower stresses in comparison with the rest. Therefore, they deformed more, through which they absorbed more energy. For the tilted-cubic: $z(y) = 0.125y - 1.0y^3$ (denoted by triangle with black outline), the blocks interlock along loading direction

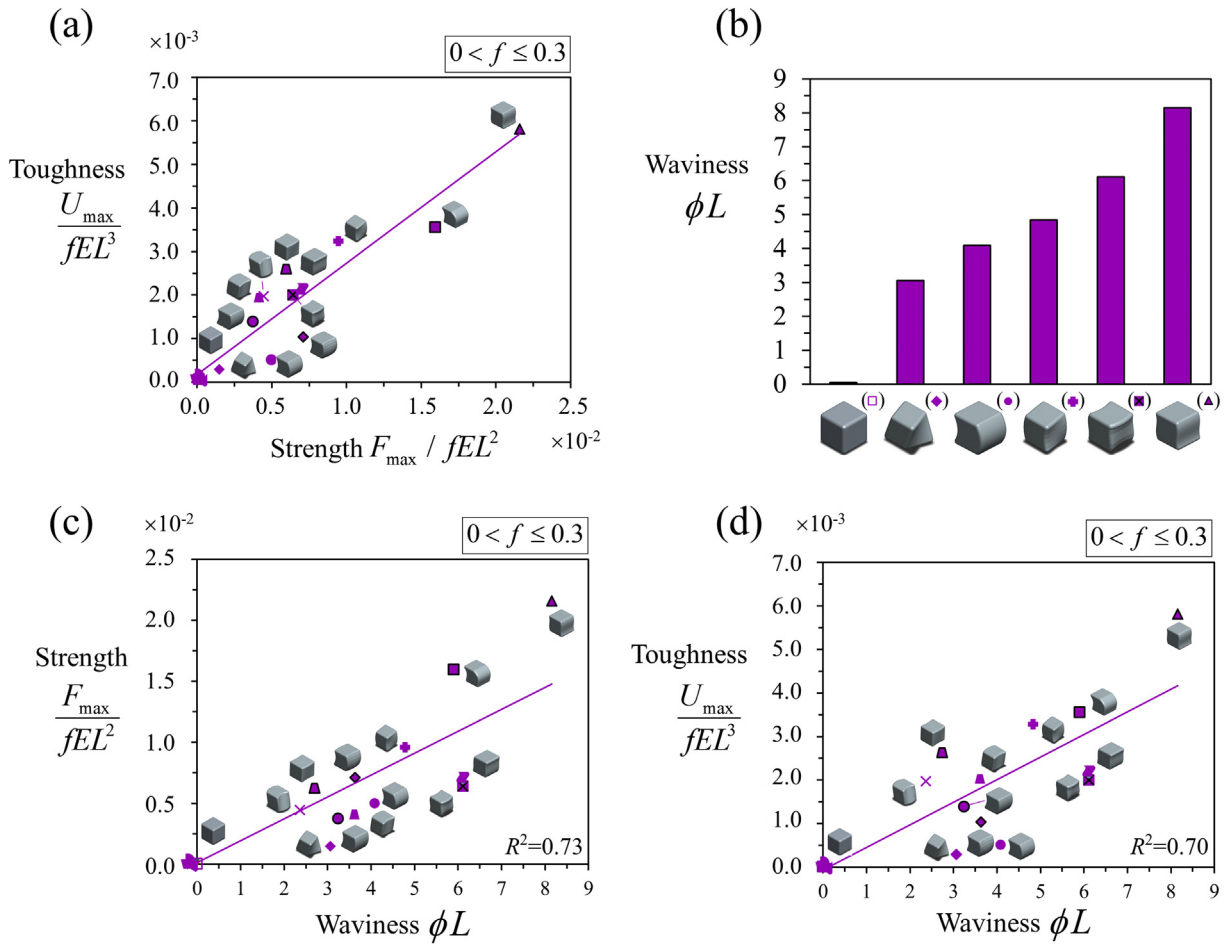


Fig. 8. (a) Normalized maximum strength F_{max} and toughness U_{max} ; (b) the geometric metric ϕL for different designs. Normalized (c) strength relationship and (d) toughness with ϕL .

(y-direction) which induces mechanical hardening and as a result fail at a higher force than the rest. Because of this interlocking it lost only 16% of strength, achieving the highest strength relative to other designs and managed to improve toughness by 4 times. For slightly stronger blocks: $\sigma_s/E = 10^{-3}$, the beam can generally sustain higher stresses, and so wavier and more curved designs are among the best designs (Fig. 11b). For highest toughness, the hyperbolic-paraboloid: $z(x,y) = a_{1,1}xy$ (denoted by a filled diamond marker) absorbed the highest energy, about 13 times more than the monolithic. Although, the cube

design performed well too, the twisted faces of hyperbolic-paraboloid guide the sliding in a twisting path along y-direction which jams the blocks and induces progressive interlocking (Appendix A.2, Fig. A.2b). For best strength, we selected two designs; the tilted-cubic denoted by a triangular marker with black outline) and the tilted-parabolic: $z(y) = 0.156y - 0.625y^2$ (denoted by a circular marker with black outline), both of which approached the strength of the monolithic. The tilted-parabolic contact face is a further enriched version of the concavo-convex design (indicated by filled circle marker), the

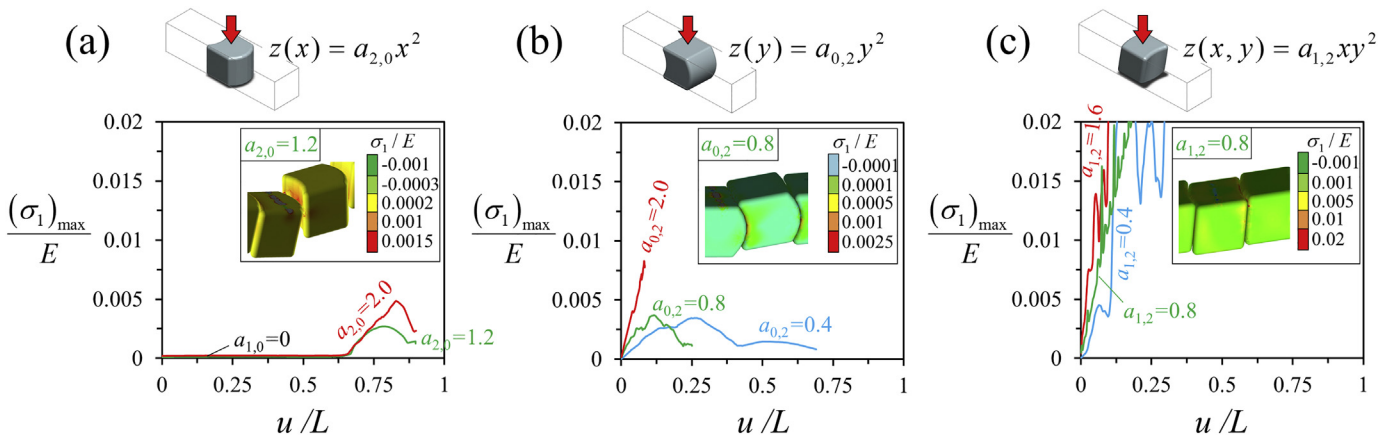


Fig. 9. Maximum principal stress during deformation for (a) $z(x) = a_{2,0}x^2$, (b) $z(y) = a_{0,2}y^2$ and (c) $z(x,y) = a_{1,2}xy^2$. The plots are reported for $f = 0.12$.

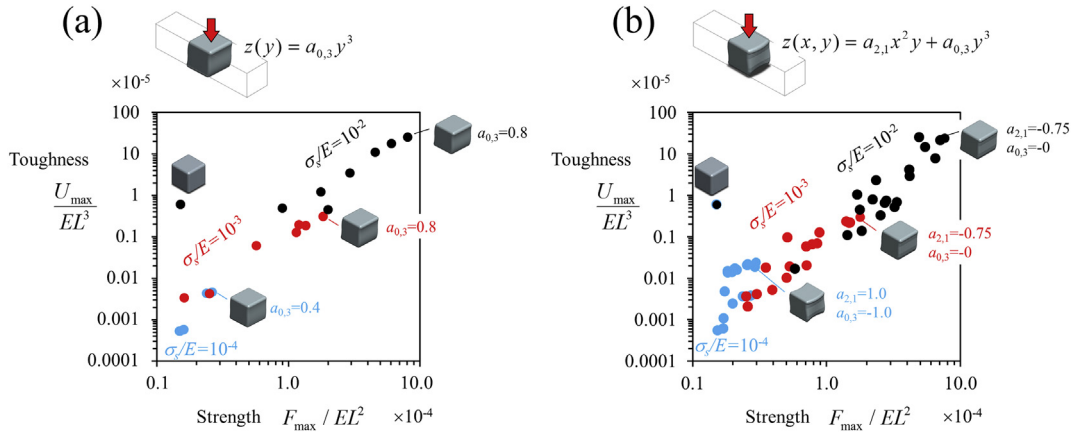


Fig. 10. Optimization of (a) a monomial: $z(y) = a_{0,3}y^3$ and (b) a binomial: $z(x,y) = a_{2,1}x^2y + a_{0,3}y^3$ for $\sigma_s/E = 10^{-4}, 10^{-3}$ and 10^{-2} . The plots are reported for $f = 0.12$.

additional $0.156y$ term induced an additional interlocking that improved its performance. Both designs lost only 30% and 4% of strength respectively, moreover, they have absorbed 4 times more energy than that of the monolithic.

For strong blocks: $\sigma_s/E = 10^{-2}$, only six designs out of 16 surpassed the toughness of the monolithic beam. For highest toughness, the $z(x,y) = -0.8y^3$ design (denoted by a curved solid square without outline) absorbed 3.5 more energy than that of the monolithic while losing 75% of strength. The tiled-cubic (denoted by a solid triangle with black outlines) was the strongest design, and absorbed 2.7 times more energy than the monolithic. These curved and wavy designs (highlighted in yellow) have also outperformed the concavo-convex design. Finally for comparison with recent studies in the literature, we added the performance of the osteomorphic blocks (Fig. 1b) which in previous studies showed promising results [12,14,15]. Here however, the osteomorphic geometry (denoted by a cross, “x”) was outperformed by some designs for all values of σ_s/E . Its best performance was achieved for $\sigma_s/E = 10^{-3}$ (Fig. 11b), where it absorbed 6 times more energy than the monolithic and lost about 65% of strength.

For weak blocks (low σ_s/E), toughness relies mainly on stability. As σ_s/E increases, toughness relies progressively more on interlocking (jamming of block). For very strong blocks, the designs reach their full potential by reaching their maximum deformation before fracture, so they mainly fail due to instability. As a result designs that generate the highest interlocking during deformation stand out.

5. Experimental testing of architected ceramic glass

In this part of the study, we fabricated and tested architected beams made of ceramic glass, a material with several attractive properties including transparency, high strength, low thermal expansion and low cost [1,3]. The samples were cut from a monolithic ceramic glass beam ($\sigma_s = 90 \pm 8.2$ MPa, $E = 100$ GPa, so $\sigma_s/E \approx 10^{-3}$) using a nano-second pulsed laser (Model Vitrolux, Vitro Laser Solutions UG, Minden, Germany) (Appendix A.4). We fabricated and tested monolithic (Fig. 12a) and cubes-based (Fig. 12b) beams as references. Both monolithic and architected samples were tested under same loads. We also fabricated and tested beams with the best three designs we identified for $\sigma_s/E \approx 10^{-3}$ (Fig. 11b): the hyperbolic-paraboloid (Fig. 12c) (best for toughness), the tilted-parabolic (Fig. 12d) (good for strength) and the tilted-cubic (Fig. 12e) (best for strength). These architected beams were mounted on two steel ($E = 200$ GPa) supports and pre-compressed along the axial direction (z -axis) by a stiff vise. The precompression force F_A was measured using a low-profile force sensor (FlexiForce®, Tekscan). All experimental tests were conducted for $F_A = 30$ N. The setup was placed under a dual column stage (Admet, model

eXpert 5000, MA US), and an indenter with a nozzle head (with radius of 1.5 mm) imposed a displacement u along the transverse direction at a rate of $10 \mu\text{m/s}$ (Fig. A.4b). The transverse force F_T was measured using a 150 lbf load cell. Using this setup, we obtained the full $F_T - u$ curves until complete failure as well as performed in-situ imaging to capture the deformation stages of the architected beam. Fig. 12 shows the deformation stages of each design with increased displacement u .

The monolithic sample showed a sudden catastrophic failure from high flexural stresses in the region of the indenter and at the lower face of the beam (indicated on Fig. 12a). For the case of cubes, the middle block(s) sled gracefully until it was fully pushed out (Fig. 12b). We did not observe cracks or chip offs during deformation for the cube design because of the low stresses at the contact faces. The hyperbolic-paraboloid design progressively failed. The blocks followed a twisted sliding path which progressively jammed the blocks. In the tilted-parabolic and the tilted-cubic designs the curved contact faces induced strong jamming at the interface, so that groups of several blocks sled as one block [43](Fig. 12d and e). The high contact stresses, that developed because of jamming, generated cracks at the interfaces (Fig. 12c, d and e). However these cracks propagated in a stable fashion with increasing load, and they were confined to individual blocks. Representative $F_T - u$ curves from these experiments are shown on Fig. 13a. As expected the monolithic beams showed a rapid linear increase in F_T that ended with sudden drop that reflects their catastrophic failure. The architected beams showed more jagged increases in forces, but sustained over much larger displacements compared to the monolithic case. This sustained but “noisy” increase in force corresponds to the progressive jamming of the blocks. The structure was tested under displacement-controlled loading which leads to stable response where the structure shows multiple load drops, gradual softening and effective energy dissipation. Displacement-controlled loading therefore reveals the maximum potential of the beam. In contrast, a force-controlled loading would result in the collapse of the structure after the first peak force, which overlooks energy dissipated during softening and subsequent deformations after peak force. During sliding the axial compressive force decreases continuously, which tend to decrease the efficacy of the jamming. The competition between geometric hardening and softening from the loss of contact area results in a maximum force, followed by softening until complete failure.

Failure in structural materials translates in a loss of load carrying capacity or its function. Here the architected samples sustained multiple force drops during loading, undergoing large deformations in the process. For applications where deflection must be controlled, the first drop in force may be considered failure. However for other applications where strength and energy absorptions are more critical, these drops

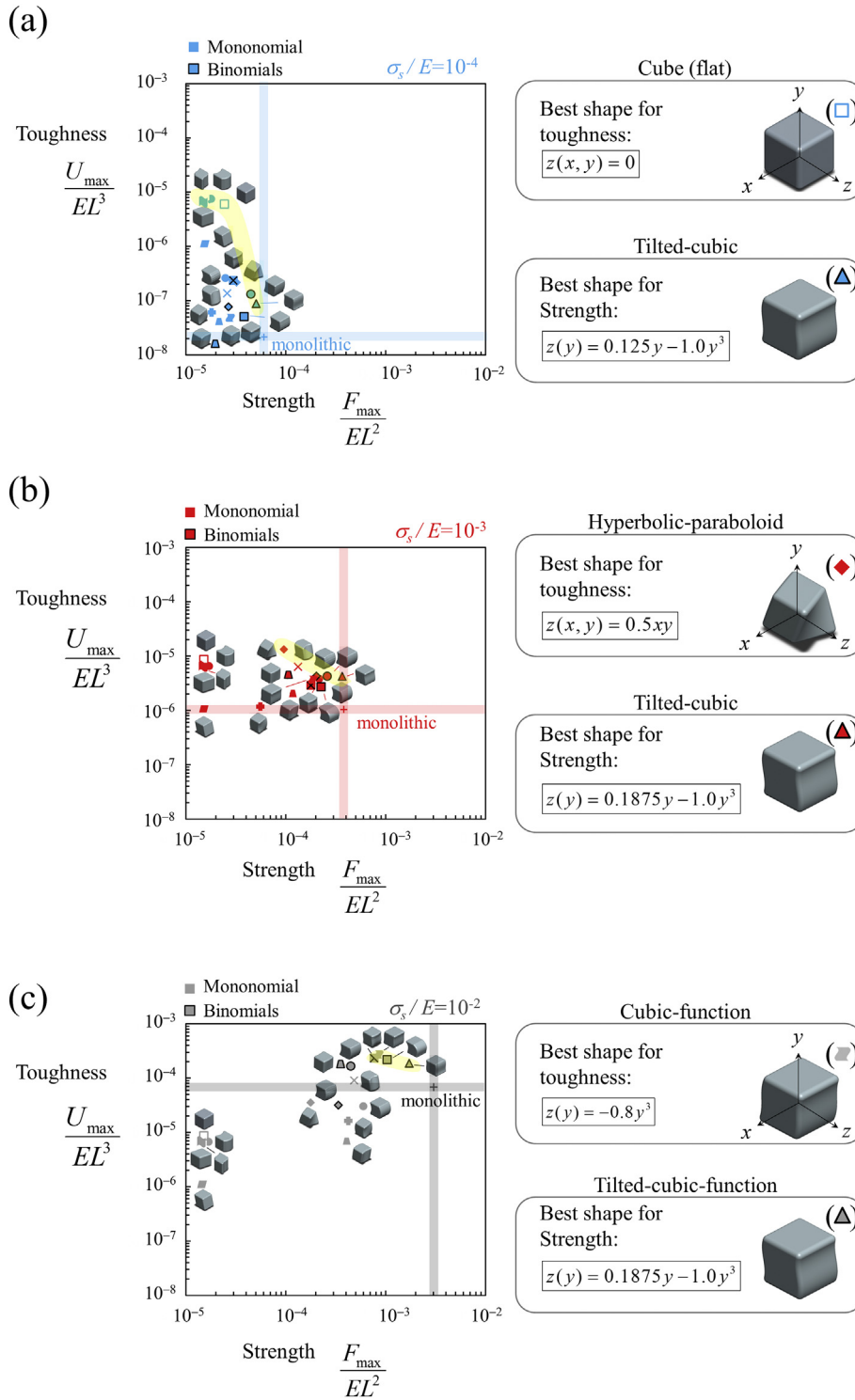


Fig. 11. Strength and toughness in an Ashby-like plot for (a) $\sigma_s/E = 10^{-4}$ (blue), (b) $\sigma_s/E = 10^{-3}$ (red), and (c) $\sigma_s/E = 10^{-2}$ (grey). The plots are reported for $f = 0.12$.

may not be considered as complete failure because the structure can still sustain increasing amounts of force, it can maintain stability, sustain deformation and absorb energy. Instead these successive force drops demonstrate a capability for damage tolerance that is absent in brittle monolithic materials. In the analysis presented here we therefore considered the full $F_T - u$ curves until complete failure at $F_T = 0$ where the curve ends, which marks the point of loss of load carrying capacity.

Using the entire experimental $F_T - u$ curves we measured strength (maximum force) and toughness (total area under the curve) for each sample ($N = 5$ for each design). These measures of strength and toughness based on entire $F_T - u$ curve serve as an appropriate estimate for maximum effective properties of the architected beam [9,21,22,41,47]. For the monolithic beam we added another measure for toughness, where we calculated the work of fracture (denoted by a dash marker, “-”) which is the energy required to grow a crack. If the

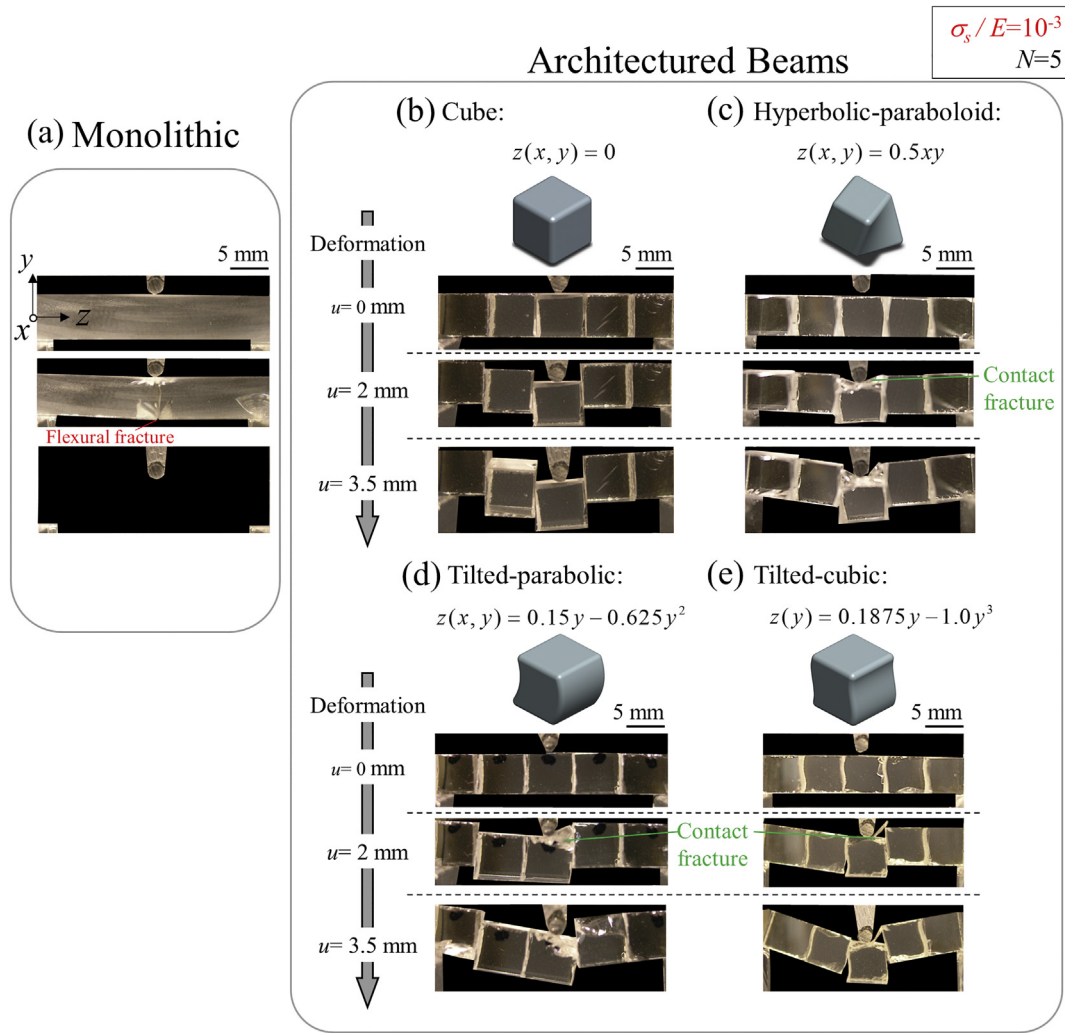


Fig. 12. Deformations of ceramic glass beams during experiments for (a) monolithic beam and architected beams: (b) $z(x, y) = 0$, (c) $z(x, y) = 0.5xy$, (d) $z(x, y) = 0.15y - 0.625y^2$ and (e) $z(x, y) = 0.1875y - 1.0y^3$.

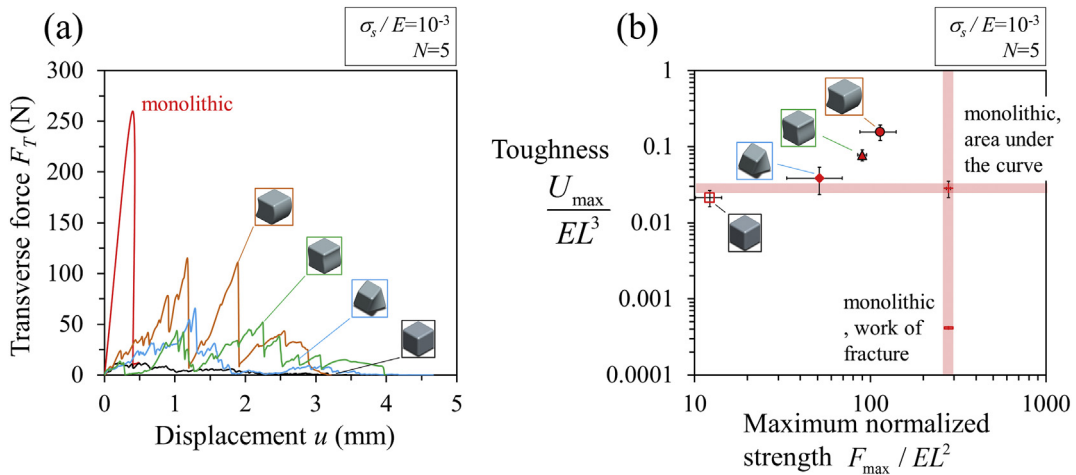


Fig. 13. Experimental data of monolithic and architected beams. (a) $F_T - u$ curves and (b) strength and toughness plotted in an Ashby-like chart. For monolithic data, toughness calculated by the total area under the $F_T - u$ curve is denoted by a cross marker, and by the work of fracture it is denoted by a dash marker.

energy release rate of ceramic glass is $G = 11.13 \text{ J/m}^2$ and the total area of the fracture surface is $A \approx 1.5 L^2$, the work of fracture becomes $U = GA = 4.17 \times 10^{-4} \text{ J}$, which is only 2% of the areas under the force-displacement curve [13]. Architected beams are compared with the monolithic using an Ashby like chart for strength and toughness (Fig. 13b). Tilted-parabolic surpassed the toughness of the monolithic beam by 5.5 times, while preserving 40% of the monolithic strength. Compared to the work of fracture of the monolithic beam, the toughness of the tilted-parabolic was 370 times higher. The tilted-cubic achieved a toughness that is 2.8 times higher, while in terms of work of fracture it is 190 times higher than that of the monolithic and with strength that is 32% of the monolithic strength. The hyperbolic-paraboloid improved toughness by 1.35 times and lost 80% of strength. The flat cubes performed poorly in comparison: Their toughness was lower than the monolithic beam, and they lost 95% of its strength. The geometric enrichments were effective in reducing the loss in strength from 95% for flat cubes to only 32%, that is >60% decrease. Further improvement in strength can be achieved by using thin monolithic beams as protection to the architected ones, a successful strategy in panels [22,41]. Comparison of the experimental chart (Fig. 13b) with corresponding simulations (Fig. 11b) shows that the relative ranking for the cube (empty square marker), hyperbolic-paraboloid (diamond marker) and the tilted cubic designs (filled triangle marker with black outline) matches simulations. However, for tilted-parabolic design (filled circle with black outline), experiments show a slightly higher strength and toughness than the tilted-cubic design (filled triangle with black outline) which is inconsistent with the ranking of simulations. This inconsistency is partly because while the FE-models captured the onset of damage, they do not capture post-damage stages (Appendix A.2, Fig. A.2). In the experiments, some of the designs (including the tilted-parabolic design) showed an increase in force following the onset of damage, which translated into better toughness and strength. FE-simulations therefore provided a conservative measure of relative performance for the architected beams. In addition, the rough contact faces of the blocks contribute to the discrepancy between model-experiments (comparing Fig. 13b and Fig. 11b). Damaged interfaces may also have lower effective Young's modulus at the contact between blocks [19], which is not the case in the simulation where we assumed constant elastic modulus for contact. Although simulations in section 8 suggested that the benefit of segmentation in comparison with monolithic beam diminishes with very large values of σ_s/E , experiments showed clearly that despite substantial damage at the surfaces, the structure can still withstand load and exhibit graceful deformation and failure.

6. Summary

In this study we have used finite element modeling and systematic geometrical enrichments to explore how interlocking and progressive jamming can be used to build strong and tough segmented beams. The simulations revealed that there are optimum shapes for the interfaces between the blocks, and that the optimum geometry depends on the normalized strength σ_s/E for the individual blocks. More specifically, the conclusions for this study are as follows:

1. Architected beams made from simple cubes with flat faces lack hardening because of the absence of jamming and/or interlocking of blocks. Adding fillets at the corner of the cubes reduced local stresses, but decreased stability. Strength and toughness depended on r/L ; where optimum r/L values are $r/L = 0.05$ and 0.025 for highest toughness and strength respectively.
2. Interlocking of blocks and jamming can be generated by enriching the contact surface along the direction of loading (i.e. the surface followed the equations of the form $z(y)$ or $z(x,y)$). Geometric

hardening can be tuned by increasing the "waviness" of the interface, but this increase also generated higher contact and frictional stresses.

3. We characterized the geometry of the blocks with a single waviness parameter $\phi L = \frac{1}{L} (\frac{\partial^2 z}{\partial y^2} + \frac{\partial^2 z}{\partial y \partial x}) / (\frac{\partial z}{\partial y} + \frac{\partial z}{\partial x})$. Assuming infinite strength of the blocks, beam strength and toughness correlated well with this waviness parameter.
4. Overall strength and toughness of the architected beams depend on the strength of the individual blocks σ_s/E . Beams made of weak material can only achieve high toughness through deformation and negligible interlocking. Beams made of stronger blocks (higher σ_s/E) can use more interlocking between blocks to achieve both high strength and toughness.
5. Experiments with ceramic glass beams made from tilted-parabolic: $z(y) = 0.15y - 0.625y^2$ and tilted-cubic: $z(y) = 0.1875y - 1.0y^3$ confirmed that these designs lead to graceful sliding and jamming of individual blocks. These designs improved toughness up to 370 times and 190 times respectively while preserving 40% and 32% of the strength of the monolithic beam respectively.

Future work may include investigating the waviness parameter ϕL in two dimensional architected panels. The systematic enrichment of the contact interfaces provides general guidelines for the strength and toughness of sliding segmented systems based on a geometric parameter (waviness). The waviness parameter successfully reflects the level of interlocking between the blocks, a key mechanism in architected materials and in engineering systems. This generic parameter may serve as objective function for future optimization problems for architected materials and as a measure of interlocking and jamming of components used in the design of engineering systems. The analysis here may remain valid for different number of blocks provided the system fails by sliding. However, we anticipate a proportional decrease in maximum strength, attributed to decrease in stiffness with larger number of blocks, therefore optimum designs and their ranking may not be affected with variations in N . This study may also provide insights on the mechanics of spines and how vertebrae interact. For synthetic materials we seek ways to increase jamming of blocks to improve strength. However, the opposite is sought to prevent spine injuries, where we seek ways to reduce the stresses. For example, by reducing the amplitude of the articulation between vertebrae (by reducing a_{ij}), reducing the slenderness (by decreasing the number of blocks), reducing the gradients of contact faces (by decreasing ϕL) and if geometrical changes are inaccessible, the vertebrae could be reinforced to increase its strength (higher σ_s/E).

Data availability

The raw/processed data required to reproduce these findings cannot be shared at this time as the data also forms part of an ongoing study.

Declaration of Competing Interest

The authors declare that they have no known competing financial interests or personal relationships that could have appeared to influence the work reported in this paper.

Acknowledgements

This work was supported by a Strategic Grant (STPGP 479137-5) from the Natural Sciences and Engineering Research Council of Canada and by a Team Grant (191270) from the Fonds de Recherche du Québec – Nature et Technologies. A.D. was partially supported by a McGill Engineering Doctoral Award.

Appendix A. Appendix

A.1. Details of finite element model

A 3-dimensional (3D) finite element models are prepared to capture the mechanical response of various interface designs. A generic code was written in Matlab to automatically enrich the blocks with different interface geometries. The models are solved in ANSYS where displacements, forces and stresses are obtained and finally post processed using Matlab. The communication between ANSYS and Matlab is automated as a single function, where different combinations of friction f , different shapes (Figs. 5 and 6) (different polynomial functions, Eq. (1)), different coefficients, precompression F_A and number of blocks N can be input and simulated. However, we have limited the study to 5 blocks ($N = 5$) because of expensive computational costs with larger N . The blocks are modeled as continuum with linear elastic model for the material with Young's modulus E and Poisson's ration $\nu = 0.2$ (typical for ceramics and brittle materials). We meshed the blocks using 20 nodes quadratic 3D element (SOLID186 [48]). The faces of the interfaces are meshed using quadratic contact elements (CONTA 172) which model contact deformations and dry contact friction. The beam rests on rigid supports. These rigid supports are meshed using rigid contact elements (TARGE 169, [49]). The blocks were pressed axially together by an axial force F_A applied at both ends ($z = 0$ and at $z = 5L$) (Fig. 2). A transverse force F_T is applied at the center of the beam at ($x = L/2$, $y = L/2$ and $z = 5L/2$). Upon solving the model, we obtain the force displacement curve $F_T - u$ and the maximum principle stress $(\sigma_1)_{\max}$. While tracking $(\sigma_1)_{\max}$ we excluded the stresses under load F_T because the stress there approach extremely large values. $F_T - u$ curves obtained from the FE model are validated against experiments for three cases of amplitude $A/L = 0$ (cube), 0.225, 0.5 for $z(y) = a_{0,2}y^2$ (Fig. A.1a). In addition, the deformation is compared with 3D printed blocks (Fig. A.1b). Fig. A.1 shows that FE simulations captured the force and the deformation of the experiments well.

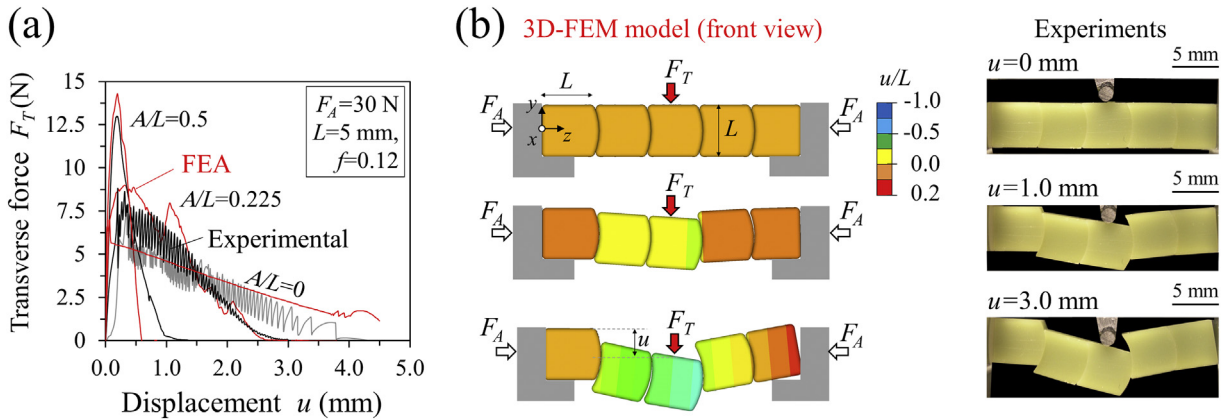


Fig. A.1. Validation of the FE-model; (a) experimental force–displacement (denoted by black line and grey; the grey colour is used to allow visualization of $A/L = 0$ case) curves compared with FE-model (denoted by a red line), (b) shows the deformation of architected beam with blocks having contact faces described by $z(y) = a_{0,2}y^2$, the deformed contour plots are compared side by side with experimental snapshots of the same design.

A.2. Calculating the strength and toughness

The maximum principal stress $(\sigma_1)_{\max}$ is tracked for the entirety of the simulation until complete failure of the system. Fig. A.2a shows the normalized stress plotted with deformation u for the hyperbolic-paraboloid: $z(x,y) = a_{1,1}xy$. Fig. A.2a shows how the displacement at a critical stress level is found. For example, here we consider the stress limit as $\sigma_s/E = 10^{-3}$ which limits the displacement at $u/L = 0.2$ which is the displacement at fracture. Fig. A.2b shows the principal stress $\sigma_1(x, y, z)$ contours at that fracture displacement ($u/L = 0.2$). Fig. A.2b also shows a zoomed image focused at the location of critical maximum stress $(\sigma_1)_{\max}$. The displacement at which $(\sigma_1)_{\max}/E > \sigma_s/E$ can then be used to truncate the force displacement curve to depict the failure of the structure (Fig. A.2c). Once the curve is truncated, we can calculate the area under the curve and the maximum force to estimate the toughness and strength respectively (Fig. A.2d).

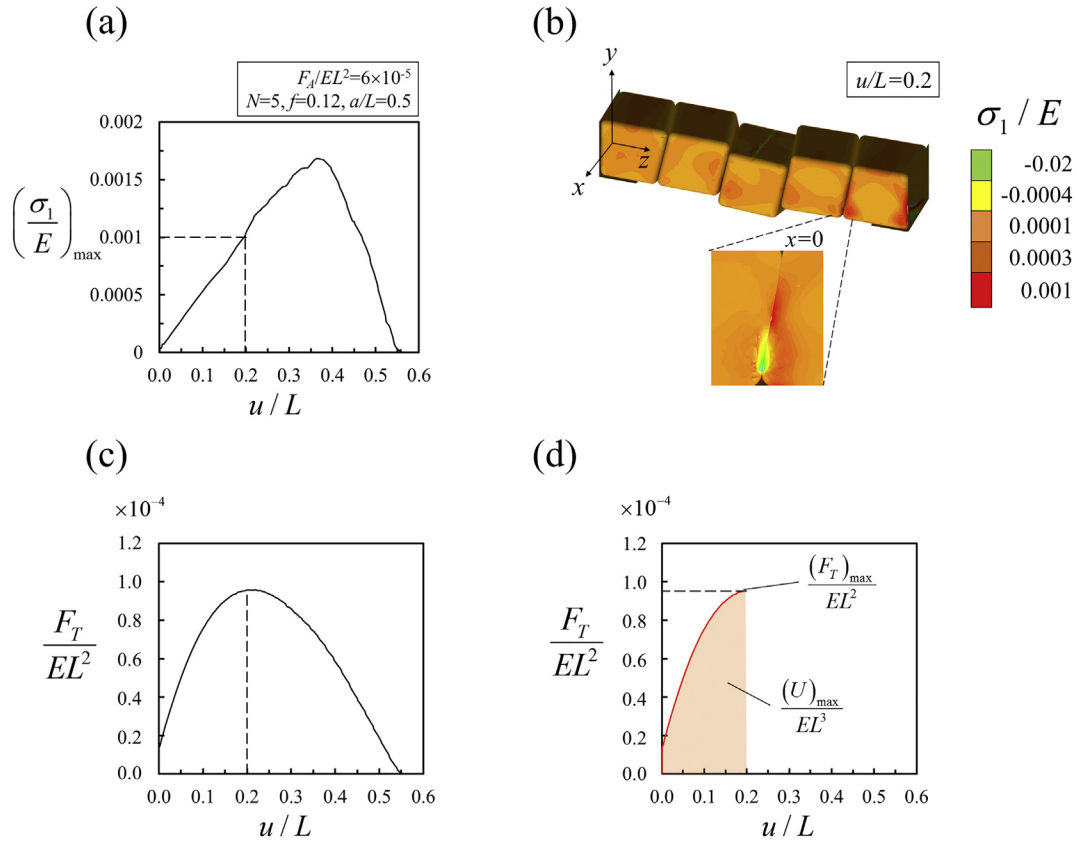


Fig. A.2. Procedure for calculating the maximum strength and toughness based on the limits of the strength of blocks σ_s/E , (a) maximum principal stress $(\sigma_1)_{\max}$ variation with displacement; displacement at the point of fracture can be found, here for example, displacement at fracture is $u/L = 0.2$ for $\sigma_s/E = 10^{-3}$; (b) contour plot of $(\sigma_1)_{\max}$ at the point of fracture; (c) force–displacement truncated, $F_T - u$; (d) $F_T - u$ truncated at the point of fracture, therefore toughness U_{\max} and strength F_{\max} are found.

A.3. Optimization of monomials and binomials

We used the procedure in Appendix A.2 to compute maximum strength F_{\max} and toughness U_{\max} for all designs shown on Figs. 5 and 6. Here we conducted a brute force optimization where we explore the design space by computing F_{\max} and U_{\max} for $\sigma_s/E = 10^{-4}$, 10^{-3} , 10^{-2} for different values of a_{ij} such that the amplitude is $A/L < 0.5$. For binomials, we explore the design space for different possible combinations of a_{ij} . For example, for the monkey-saddle: $z(x,y) = a_{2,1}x^2y + a_{0,3}y^3$, combinations of $(a_{2,1}, a_{0,3})$ is simulated for the range of $[0,1]$ and $[-1,1]$ with increment of 0.25, which results in 25 simulations for each σ_s/E value and a total of 75 simulations for each design. $a_{2,1}$ starts from 0 because the design space within the range of $[-1,0]$ and $[-1,1]$ for $a_{2,1}$ and $a_{0,3}$ respectively is identical to the $[0,1]$ and $[-1,1]$, so part of the design space bound by $a_{2,1}$ with $[-1,0]$ is redundant. As an example, Fig. A.3 shows F_{\max} and U_{\max} for different a_{ij} values for $z(y) = a_{0,3}y^3$ and $z(x,y) = a_{2,1}x^2y + a_{0,3}y^3$.

Fig. A.3a shows that F_{\max} and U_{\max} increases as $a_{0,3}$ increases because of increased geometric hardening resulting from larger $a_{0,3}$. However, there is a peak point after which both F_{\max} and U_{\max} start to decrease. Fig. A.3b shows F_{\max} and U_{\max} as contours for $\sigma_s = 10^{-3}$ because the simulation is run for 2 design variables: $a_{2,1}$ and $a_{0,3}$. Strength is maximum at $(a_{2,1} = 0.75, a_{0,3} = 0)$, for this particular design any contribution from $a_{0,3}$ term induces severe interlocking between blocks which results in very high stresses. These high stresses exceed σ_s/E of the beam therefore the maximum force reached during deformation is lower than cases of $a_{0,3} = 0$. Whereas, toughness is maximum at $(a_{2,1} = 0, a_{0,3} = 0)$ which represents the cubes case. The cubes contact faces are flat, so the stresses are much lower than wavy and curved faces, therefore it can deform for larger displacement without failure. Both Fig. A.3a and b shows how peak points for F_{\max} and U_{\max} may not necessary match, because there is a compromise between strength and toughness where both can have their distinct optimum a_{ij} values. The objective is to find the optimum design for both strength and toughness. To do so we plot simulation results on $F_{\max} - U_{\max}$ space. If the strength and toughness of a particular design is greater than the rest, this design is therefore is nondominated and it is considered as an optimum design. Optimum designs is shown adjacent to their corresponding optimum points.

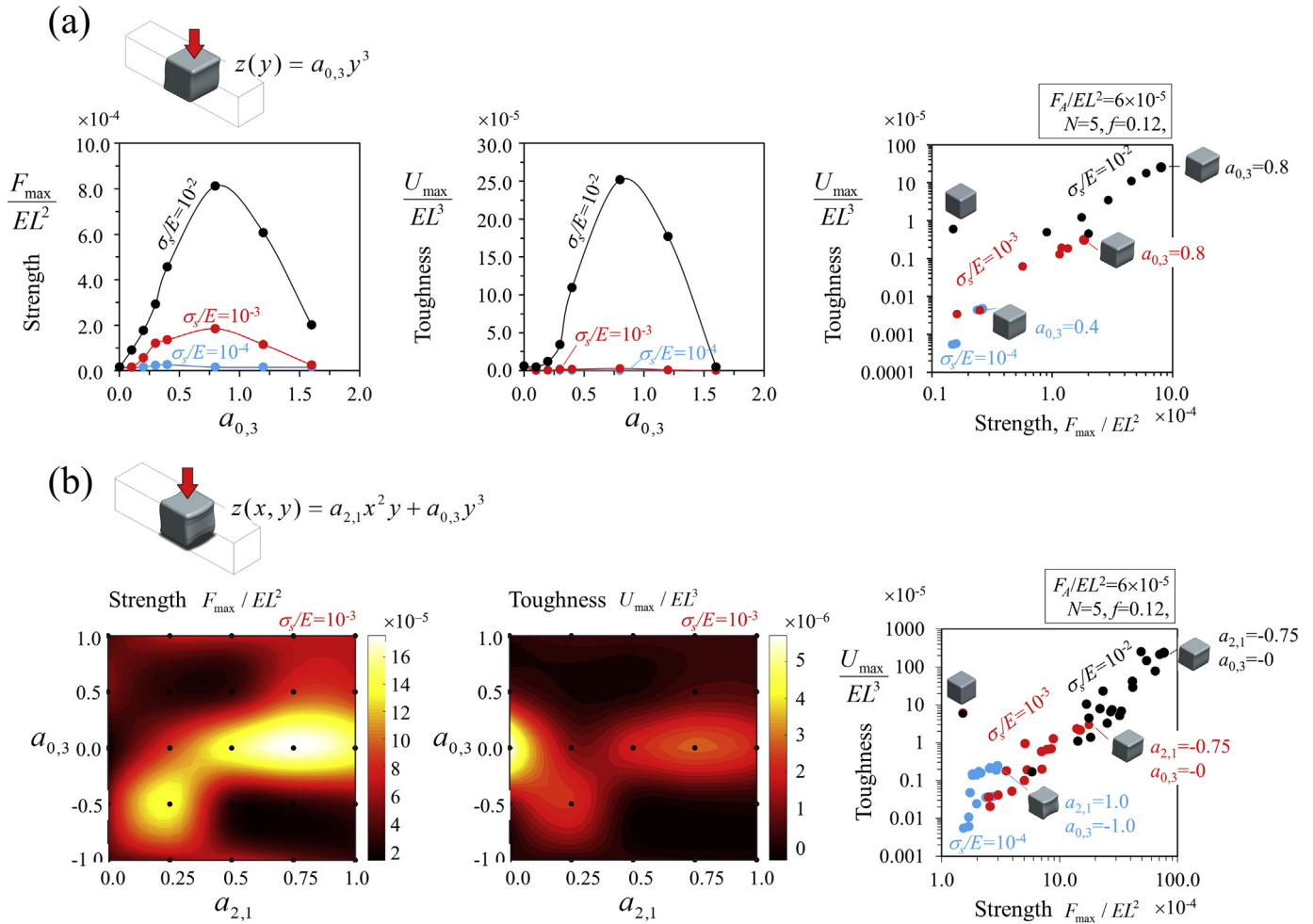


Fig. A.3. Brute force optimization for the coefficients a_{ij} such that the $A/L \leq 0.5$ for (a) a monomial: $z(y) = a_{0,3}y^3$ and (b) a binomial: $z(x, y) = a_{2,1}x^2y + a_{0,3}y^3$.

A.4. Preparing the ceramic glass samples

A 50 mm × 50 mm × 5 mm ceramic glass plate is cut into several prismatic beams with a span of 25 mm and depth of 5 mm (Fig. A.4a). These beams are cut into unit blocks using a nanosecond laser (Model Vitrolox, Vitro Laser Solutions UG, Minden, Germany) equipped with a pulsed UV laser (355 nm, 0.5 W cw pumped, 4 kHz repetition rate, 4–5 ns pulse duration). Different shapes were input as a cloud of points described by Eq. (1). The laser therefore traces different geometries and so carves the desired shapes of blocks from the prismatic beams (Fig. A.4b). The blocks are then assembled into an architected beam and mounted on steel rigid supports ($E = 250$ GPa) (Fig. A.4b). The blocks are pressed by a vise from both ends. A low-profile pressure sensor tracks and measures the axial force before and during testing. A dual-column loading stage (Admet, model eXpert 5000, MA US) is used to apply a displacement control load along the transverse direction (y -axis) by an indenter with a round nozzle head of a radius $R = 1.5$ mm. The displacement is imposed at a rate of $10 \mu\text{m/s}$ at the center of the beam (half way along the span) until complete failure. The transverse force F_T was measured using a 150 lbf load cell.

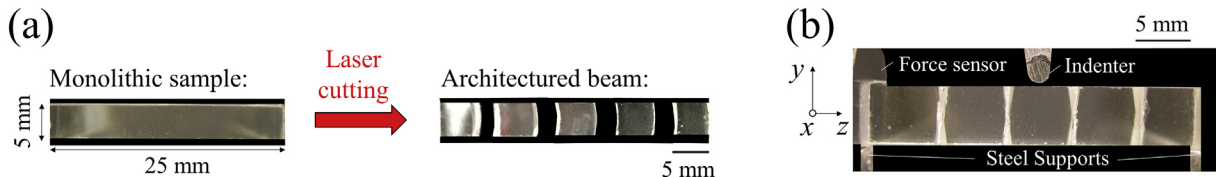


Fig. A.4. Experimental testing and fabrication of architected ceramic glass beams. (a) monolithic beam is laser cut into blocks; (b) experimental setup.

A.5. Application of precompression in real systems

Linearly segmented architected materials can be used as structural components as beams and columns. To apply axial compression on architected beams without interfering with large deformation, sliding and rotation of blocks, the component can rest on a fixed support at one end and on a variable spring support [27] at the other end. This configuration provides a practical control over strength and toughness as function of axial compression F_A .

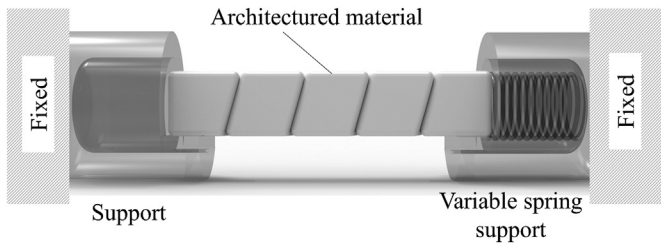


Fig. A.5. An example of precompression setup for architected beams using variable spring support.

References

- [1] M.F. Ashby, *Materials Selection in Mechanical Design*, 5 ed. Butterworth-Heinemann, Cambridge, MA, 2016.
- [2] L. Wondraczek, J.C. Mauro, J. Eckert, U. Kühn, J. Horbach, J. Deubener, et al., Towards ultrastrong glasses, *Adv. Mater.* 23 (2011) 4578–4586.
- [3] J.B. Wachtman, W.R. Cannon, M.J. Matthewson, *Mechanical Properties of Ceramics*, John Wiley & Sons, 2009.
- [4] R.E. Klingner, *Masonry Structural Design*, McGraw-Hill Professional Publishing, New York, USA, UNITED STATES, 2010.
- [5] A. Schultz, M. J. Scolforo, An overview of prestressed masonry, *TMS J.* 10 (1991) 6–21.
- [6] K.G. Sharp, P.J. Armstrong, *Interlocking Concrete Block Pavements*, Australian Road Research Board Special Report, 1985.
- [7] A.V. Dyskin, Y. Estrin, A.J. Kanel-Belov, E. Pasternak, Toughening by fragmentation—how topology helps, *Adv. Eng. Mater.* 3 (2001) 885–888.
- [8] A.V. Dyskin, Y. Estrin, A.J. Kanel-Belov, E. Pasternak, Topological interlocking of platonic solids: a way to new materials and structures, *Philos. Mag. Lett.* 83 (2003) 197–203.
- [9] T. Siegmund, F. Barthelat, R. Cipra, E. Habtour, J. Riddick, Manufacture and mechanics of topologically interlocked material assemblies, *Appl. Mech. Rev.* 68 (2016), 040803.
- [10] M. Mirkhalaf, A. Sunesara, B. Ashrafi, F. Barthelat, Toughness by segmentation: fabrication, testing and micromechanics of architected ceramic panels for impact applications, *Int. J. Solids Struct.* 158 (2019) 52–65.
- [11] M. Mirkhalaf, T. Zhou, F. Barthelat, Simultaneous improvements of strength and toughness in topologically interlocked ceramics, *PNAS* 115 (2018) 9128–9133.
- [12] A. Rezaee Javan, H. Seifi, S. Xu, X. Lin, Y.M. Xie, Impact behaviour of plate-like assemblies made of new and existing interlocking bricks: a comparative study, *Int. J. Impact Eng.* 116 (2018) 79–93.
- [13] G.T. Camacho, M. Ortiz, Computational modelling of impact damage in brittle materials, *Int. J. Solids Struct.* 33 (1996) 2899–2938.
- [14] A.V. Dyskin, Y. Estrin, E. Pasternak, H.C. Khor, A.J. Kanel-Belov, The principle of topological interlocking in extraterrestrial construction, *Acta Astronaut.* 57 (2005) 10–21.
- [15] A.V. Dyskin, Y. Estrin, E. Pasternak, H.C. Khor, A.J. Kanel-Belov, Fracture resistant structures based on topological interlocking with non-planar contacts, *Adv. Eng. Mater.* 5 (2003) 116–119.
- [16] H. Ming-Yuan, J.W. Hutchinson, Crack deflection at an interface between dissimilar elastic materials, *Int. J. Solids Struct.* 25 (1989) 1053–1067.
- [17] F. Barthelat, Architected materials in engineering and biology: fabrication, structure, mechanics and performance, *Int. Mater. Rev.* 60 (2015) 413–430.
- [18] M. Mirkhalaf, A.K. Dastjerdi, F. Barthelat, Overcoming the brittleness of glass through bio-inspiration and micro-architecture, *Nat. Commun.* 5 (2014).
- [19] J. Kemeny, N.G.W. Cook, Effective moduli, non-linear deformation and strength of a cracked elastic solid, *Int. J. Rock Mech. Min. Sci. Geomech. Abstr.* 23 (1986) 107–118.
- [20] I.A. Malik, F. Barthelat, Toughening of thin ceramic plates using bioinspired surface patterns, *Int. J. Solids Struct.* 97–98 (2016) 389–399.
- [21] S. Khandelwal, T. Siegmund, R.J. Cipra, J.S. Bolton, Transverse loading of cellular topologically interlocked materials, *Int. J. Solids Struct.* 49 (2012) 2394–2403.
- [22] Z. Yin, F. Hannard, F. Barthelat, Impact-resistant nacre-like transparent materials, *Science* 364 (2019) 1260–1263.
- [23] G. Grimaldi, A. Papangelo, M. Ciavarella, A Cattaneo-Mindlin problem for a rigid punch with tangential load applied above the interface line, *Proc. Inst. Mech. Eng. C J. Mech. Eng. Sci.* 230 (2016) 1410–1416.
- [24] K.L. Johnson, *Contact Mechanics*, Cambridge University Press, 1987.
- [25] P.J. Blau, *Friction Science and Technology*, CRC Press, 1995.
- [26] Y. Estrin, Y. Bréchet, J. Dunlop, P. Fratzl, *Architected Materials in Nature and Engineering*: Archimats, Springer International Publishing, 2019.
- [27] T. Davidson, C. Cunneen, in: S. United (Ed.), *Variable Spring Hanger Assembly*, F AND S Manufacturing CORP, 1979.
- [28] F. Barthelat, Biomimetics for next generation materials, *Philos. Trans. R. Soc. Lond. A* 365 (2007) 2907–2919.
- [29] Z. Liu, M.A. Meyers, Z. Zhang, R.O. Ritchie, Functional gradients and heterogeneities in biological materials: design principles, functions, and bioinspired applications, *Prog. Mater. Sci.* 88 (2017) 467–498.
- [30] S. Alben, P.G. Madden, G.V. Lauder, The mechanics of active fin-shape control in ray-finned fishes, *J. R. Soc. Interface* 4 (2007) 243–256.
- [31] M.E. Porter, R.H. Ewoldt, J.H. Long, Automatic control: the vertebral column of dogfish sharks behaves as a continuously variable transmission with smoothly shifting functions, *J. Exp. Biol.* 219 (2016) 2908–2919.
- [32] I.F. Dunn, M.R. Proctor, A.L. Day, Lumbar spine injuries in athletes, *Neurosurg. Focus.* 21 (2006) E4.
- [33] T.R. Oxland, Fundamental biomechanics of the spine—what we have learned in the past 25 years and future directions, *J. Biomech.* 49 (2016) 817–832.
- [34] P. Fratzl, O. Kolednik, F.D. Fischer, M.N. Dean, The mechanics of tessellations - bioinspired strategies for fracture resistance, *Chem. Soc. Rev.* 45 (2016) 252–267.
- [35] N. Clement, R. Schlader, Orcinus orca, Idha Virtualization Laboratory, 2012.
- [36] J.K. Wright, Ammonites, *Geol. Today* 28 (2012) 186–191.
- [37] J.S. John, Tornoceras Uniangular Aldenense Fossil Goniatite (Alden Pyrite Bed, Ludlowville Formation, Middle Devonian; Western New York State, USA), 2014 1.
- [38] J.A. Fronimos, J.A. Wilson, T.K. Baumiller, Polarity of concavo-convex intervertebral joints in the necks and tails of sauropod dinosaurs, *Paleobiology* 42 (2016) 624–642.
- [39] E.L. Troxell, Mechanics of crocodile vertebræ, *GSA Bull.* 36 (1925) 605–614.
- [40] J.L. Molnar, S.E. Pierce, A.S. Bhullar, A.H. Turner, J.R. Hutchinson, Morphological and functional changes in the vertebral column with increasing aquatic adaptation in crocodylomorphs, *Open Sci.* 2 (2015) 150439.
- [41] A.S. Dalaq, F. Barthelat, Three-dimensional laser engraving for fabrication of tough glass-based bioinspired materials, *JOM* 72 (2020) 1487–1497.
- [42] B.-Y. Luo, W.-L. Goh, Z. Chen, J.-M. Yuan, Laterally pre-compressed SiC tiles against long rod impact, *Def. Technol.* 14 (2018) 585–589.
- [43] A.S. Dalaq, F. Barthelat, Strength and stability in architected spine-like segmented structures, *Int. J. Solids Struct.* 171 (2019) 146–157.
- [44] M. Mirkhalaf, J. Tanguay, F. Barthelat, Carving 3D architectures within glass: exploring new strategies to transform the mechanics and performance of materials, *Extreme Mech. Lett.* 7 (2016) 104–113.
- [45] J. Géraudie, A. Brullfert, M.J. Monnot, P. Ferretti, Teratogenic and morphogenetic effects of retinoic acid on the regenerating pectoral fin in zebrafish, *J. Exp. Zool.* 269 (1994) 12–22.
- [46] J. Stewart, *Calculus*, Cengage Learn., Cengage Learning, 2011 6th Edition, pg. 832–834.
- [47] L. Djumas, G.P. Simon, Y. Estrin, A. Molotnikov, Deformation mechanics of non-planar topologically interlocked assemblies with structural hierarchy and varying geometry, *Sci. Rep.* 7 (2017), 11844.
- [48] ANSYS (Ed.), *ANSYS Mechanical APDL Modeling and Meshing Guide*, 2013, November 2013 ed: ANSYS, Release 15.0.
- [49] ANSYS, *ANSYS Mechanical APDL Contact Technology Guide*, ANSYS, Release 15.0 2013.